Progress In Electromagnetics Research C, Vol. 126, 157–172, 2022

A 3D Multi-Rays Path Loss Model above 6 GHz under Indoor Environments with Regular Structures

Yu Yu*, Ting-Ting Liu, Yong-Qiang Bao, Heng-Fei Xu, Shu Jiang, and Wen-Hao Zeng

Abstract—An analytical multi-rays path loss model with low complexity and high accuracy is proposed to realize the ubiquitous communication links with solid stability and full coverage. The closed-form formulas are derived to describe the path loss above 6 GHz under regularly-structured indoor environments, ensuring a clear propagation mechanism and low computational complexity. In this model, the construction and destruction of the dominant rays, i.e., the direct, reflected, diffracted, diffracted-reflected, and reflected-reflected rays, on the path loss, are considered according to variation of the transmitting antenna position and propagation condition. The proposed model contains information on the sizes, structures, and materials of the environments and eliminates the influences of small scale fading by averaging the path loss over a circle with radius of ten wavelengths. Based on the measurements under the "L-shaped" corridor and office environments at 8 GHz band, the accuracy and extensibility of the proposed path model are verified. This work can help analyze the propagation mechanisms and construct the solver for calculating the attenuation of electromagnetic waves under indoor environments. It can also provide vital information for the link budget and node deployment for future wireless communication systems above 6 GHz.

1. INTRODUCTION

Ubiquitous communications become crucial in the fifth (5G) and sixth (6G) generation mobile communication systems to enhance the user experience [1, 2]. A key to realizing ubiquitous communications is deploying indoor short-range communication links in small spaces such as offices and corridors [3]. In fact, the propagation characteristic, in particular path loss, is a significant concern in deploying these links. However, the frequency bands below 6 GHz are congested due to the popularity of the existing communication technologies [4]. Therefore, future communication systems should take high frequency bands beyond 6 GHz into consideration. Thus, an accurate path loss model above 6 GHz for ubiquitous communications is strongly desired.

The issue of path loss modeling under different indoor environments has received considerable attention [5–8]. The path loss models can be classified into three types: measurement-based path loss models, theoretical path loss models, and Ray Tracing (RT) based path loss models. Table 1 lists some representative work. The measurement-based path loss models, also known as empirical path loss models, are primarily concerned with determining the proper form of the path loss model and its correction terms based on extensive measured data. There are many widely-used empirical path loss models, including the log-distance, dual-slopes, Close-In (CI), Close-In with Frequency Dependent Exponent (CIF), Close-In with Height Dependent Exponent (CIH), Alpha-Beta-Gamma (ABG), Multi-Wall Multi-Floor (MWMF), and ITU-R indoor P.1238-10 models [9]. The amount of literature on terahertz and millimeter wave path loss models has become popular recently. In [10], the CI model with a

Received 30 July 2022, Accepted 31 October 2022, Scheduled 9 November 2022

* Corresponding author: Yu Yu (yuyu@njit.edu.cn).

The authors are with the School of Information and Communication Engineering, Nanjing Institute of Technology, Hongjing Avenue 1, Nanjing 211167, China.

Table 1. The representative related works.

Literature	Data Collection Method	Frequency	Environment	Model
[10]	Measurements	4.5, 28, 38 GHz	Ground floor	CIF
[11]	Measurements	28, 73, 140 GHz	Indoor office building	CI, CIF
[12]	Measurements	140–220 GHz	Office	Log-distance Model
[13]	Measurements	28 GHz	Corridor	Dual-slopes Model
[14]	RT and measurements	2.4 GHz	Hallway	Waveguide model
[15]	Measurements	915 MHz	Factories	Improved 2-ray model
[16]	RT and measurements	38 GHz	Corridor	Ten rays model
[17]	RT	2.4 GHz	Wide corridor with glass	2D ray tracing model
[18]	RT and measurements	38 GHz	Basement floor	3D ray tracing model
[19]	RT and measurements	5, 31, 90 GHz	Different corridors	CI, FI

correction factor related to the line-of-sight (LOS) and non-LOS (NLOS) conditions was proposed based on the measured data at 4.5 GHz, 28 GHz, and 38 GHz. One investigation compared the similarity of the path loss exponents at 28, 73, and 142 GHz [11]. The path loss for the higher 140 GHz–220 GHz terahertz frequency band was described by a log-distance model [12]. Additionally, under the corridor environment with the waveguide-like structure, the impact of the environment's structure on the path loss model was further examined [13]. Also, the theoretical path loss models utilized electromagnetic theory to describe path loss under indoor environments. Previous research established an improved 2-ray path loss model to characterize the signal strength under the manufacturing environment [14]. Researchers attempted to propose a waveguide channel model to describe the attenuation coefficients of the path loss under an indoor hallway environment [15]. A great deal of research has adopted RT simulations for path loss modeling, considering multiple reflected, diffracted, and transmitted rays. Path loss in the corridor was described using a ten-ray model with multiple reflections [16]. It was experimentally demonstrated that 2D ray [17] and 3D ray tracing [18] could be used to establish path loss models. In addition, several researchers have considered the combination of the RT simulation and empirical path loss models. High agreements can be observed between the measurement and RT simulation results at 5 GHz, 31 GHz, and 90 GHz for both CI and FI models [19]. Moreover, some commercial or academic ray tracing software, i.e., Wireless InSite, Cloud RT, WinProp, COMSOL Multiphysics, etc., are widely applied for analyzing the propagation characteristics of the channel [20, 21].

The path loss model applied to ubiquitous indoor communications should consider the following aspects. Firstly, due to the extensive applications of ubiquitous communications, it is preferable to predict the path loss fast using closed-form formulas. Secondly, the dominant propagation mechanisms should be considered, given the complex multipath effects in indoor environments. Lastly, the path loss of ubiquitous transmitting and receiving points in 3D regions should be characterized because people, machines, and objects at any place can access the networks in ubiquitous communications.

However, existing path loss models are limited for the following reasons. The distance-dependent empirical path loss models cannot fully describe the path loss everywhere in 3D spaces. Although 3D RT-based models can address this issue, the process of establishing digital maps and high computational complexity will make them inefficient. Fortunately, the theoretical models can fast calculate the path loss using closed-form formulas. Nevertheless, the existing analytical models are mainly applied to simple environments. Therefore, one of the greatest challenges for constructing stable and full coverage ubiquitous communication links is establishing the closed-form path loss model with low complexity and high accuracy.

Motivated by the above challenges, we present a 3D multi-rays path loss model based on theoretical analysis in indoor environments with regular structures. The main contributions of the proposed model are listed as follows.

1) The analytical closed-form path loss model under regularly-structured indoor environments is proposed. The model parameters are the location of the transmitting antennas, sizes, materials

of the environments, and the wavelength of electromagnetic waves. The proposed model can therefore be used in a variety of frequency bands, indoor environments, and transmitting antenna deployments.

2) The proposed path loss model reveals dominant propagation mechanisms. According to the transmitting antenna positions and propagation conditions, the construction and destruction of the dominant rays, i.e., the direct, reflected, diffracted, diffracted-reflected, and reflected-reflected rays, on the path loss are considered. It takes a balance between complexity and accuracy.
3) The proposed model, which is represented as a function of the coordinates of the receiving points, can be used to characterize the path loss everywhere in 3D spaces in indoor environments. Compared with the traditional path loss model, it is helpful for ubiquitous communications in 5G and 6G communication systems.

The remainder of this paper is organized as follows. This paper begins by describing the procedure for proposing the path loss model in Section 2. To be more specific, Section 2.1 illustrates the methodology for modeling. Then, we derive the electric fields for both the LOS and NLOS conditions based on theoretical analysis in Sections 2.2–2.3. Moreover, the proposed path loss model is presented in Section 2.4. It will then go on to verify the accuracy of the proposed model in Section 3, where the measurement campaigns under an "L-shaped" corridor and office are shown in Section 3.1, and the proposed model is validated by the measured data in Section 3.2. Finally, we draw the conclusions in Section 4.

2. PROPOSED 3D MULTI-RAYS PATH LOSS MODEL

Beginning in this section, we discuss how electromagnetic waves propagate in the environment with regular structures. The detailed expression for computing the electric fields for both LOS and NLOS conditions is then derived. Finally, the closed-form 3D multi-rays path loss model is proposed.

2.1. Modeling Methodology

The following analysis and modeling are based on the structures in Fig. 1. As presented in Fig. 1, Tx and Rx denote the transmitting and receiving antennas, respectively. H, W_1, W_2, L_1, and L_2 are the sizes of the environments. It is obvious that the structure will be an "L-shaped" corridor when $W_1 \neq L_2$ and $W_2 \neq L_1$; meanwhile, it will be an office or room when $W_1 = L_2$ and $W_2 = L_1$. Thus, such structures can describe typical indoor environments, i.e., corridors, offices, rooms, etc.

The path loss at high frequency band above 6 GHz is considerable according to the free-space path loss model. For example, the free-space path loss is about 50.5 dB of 1 m distance at 8 GHz frequency band. A lot of signal energy will be dissipated with the increase in the propagation distance.

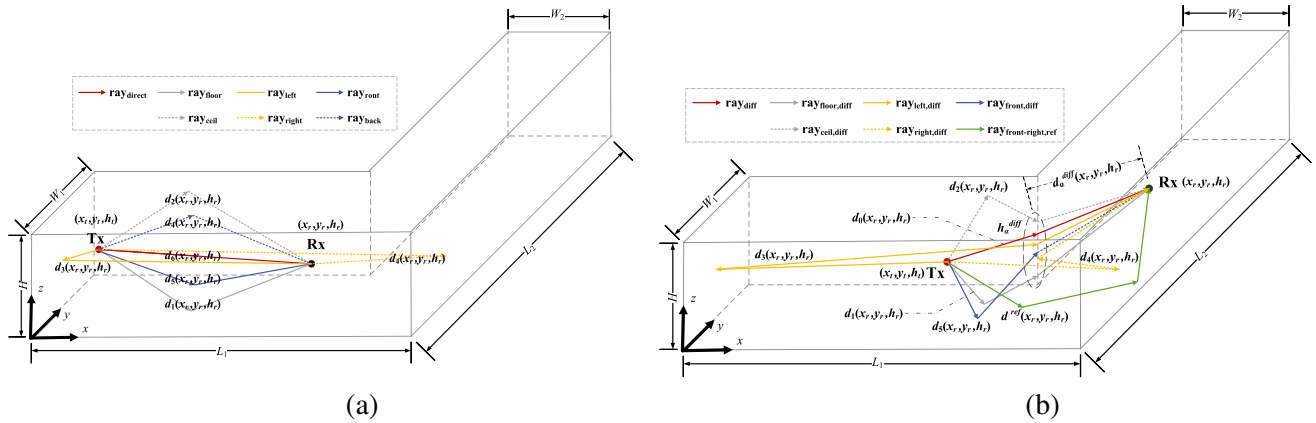

Figure 1. The structures for channel modeling: (a) LOS condition and (b) NLOS condition.

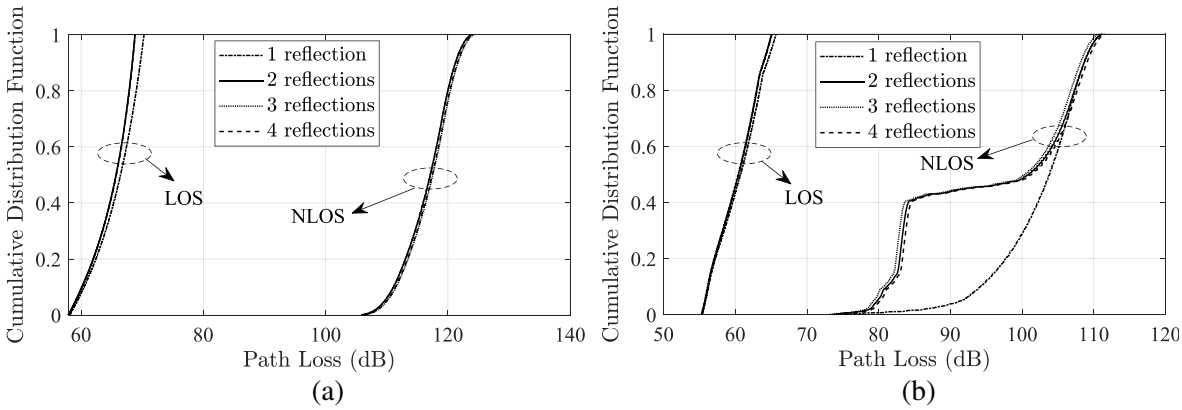

Figure 2. Path loss distributions for different numbers of reflections by ray tracing simulation: (a) the transmitting antenna is far away from the corner and (b) the transmitting antenna is near the corner.

Additionally, the reflection and diffractions of the electromagnetic waves will dramatically attenuate the signal strength [22]. We conduct the ray tracing simulations under an "L-shaped" corridor environment for both LOS and NLOS conditions to determine the order of reflections. Herein, as shown in Fig. 2, the path losses for one diffraction and different numbers of reflections are simulated. Also, the transmitting antenna is set far away from or near the corner of the "L-shaped" corridor. The simulation results show that for the LOS condition, the difference among the path losses of different numbers of reflections is small, no matter whether the transmitting antenna is far from or near the corner. Therefore, one reflection for the LOS condition is enough to describe the path loss. Meanwhile, the results are more complex for the NLOS condition. If the transmitting antenna is far from the corner, the path losses for different numbers of reflections are quite similar. Thus, one reflection should be considered in this case. If the transmitting antenna is near the corner, there is an apparent gap between the path losses of one reflection and two reflections; additionally, the differences among the path losses of two, three, and four reflections are minor. It means that two reflections can characterize the propagation characteristics under such a regular environment.

Based on the simulation, the direct ray and reflected rays from different walls are found to be dominant for the LOS condition. In Figs. 1(a) and (b), the dominant rays for both the LOS and NLOS conditions are drawn, respectively. They are the direct LOS ray (called *direct ray*) and the rays reflected by the floors, ceilings, left walls, right walls, front walls, and back walls (called *reflected rays*), which are denoted as $\text{ray}_{\text{direct}}$, $\text{ray}_{\text{floor}}$, ray_{ceil}, ray_{left}, $\text{ray}_{\text{right}}$, $\text{ray}_{\text{front}}$, and ray_{back} for the LOS conditions, respectively.

Moreover, Fig. 1(b) displays the dominant multipath components for the NLOS conditions, where Tx1 and Tx2 mean the Tx far from and near the corner, respectively. Due to the obstruction of the direct path between the transmitting and receiving antennas, the LOS ray is missing, and the main propagation mechanisms for the NLOS condition are reflection and diffraction. For the NLOS condition, the dominant rays consist of the diffracted ray (called *diffracted ray*) and the rays reflected by the walls at first and then diffracted by the corner (called *reflected-diffracted rays*) when the transmitting antenna is far from the corner. They are represented by ray_{diff}, $\text{ray}_{\text{floor, diff}}$, $\text{ray}_{\text{ceil, diff}}$, $\text{ray}_{\text{left, diff}}$, $\text{ray}_{\text{right, diff}}$, and $\text{ray}_{\text{front, diff}}$. The subscripts, i.e., floor, ceil, left, right, and front, mean the plane on which the reflection occurs. It is noteworthy that since the diffraction points are on the back wall, the electromagnetic will not be reflected by the back wall. Also, besides the above rays, we should consider the ray reflected by the front wall at first and then reflected by the right wall (called *reflected-reflected rays*) when the transmitting antenna is near the corner, which is denoted as $\text{ray}_{\text{front-right, ref}}$. This is because the ray reflected by the front and right walls is most important, and the other double-reflected rays are much smaller than the diffracted rays by ray tracing.

Based on the above analysis, in the following channel model, the propagation paths corresponding to more than one reflection for the LOS condition, as well as two reflections or one diffraction for the NLOS condition, are generally neglected for the simplicity of the model under the premise of ensuring

clear propagation mechanism and low computational complexity.

For the convenience of the following analysis and modeling, we define the following points at first:

$$\begin{aligned}
\text{original ponit}: &\quad (x_t, y_t, h_t) \to (x_0, y_0, h_0)\\
\text{floor plane image point}: &\quad (x_t, y_t, -h_t) \to (x_1, y_1, h_1)\\
\text{ceiling plane image point}: &\quad (x_t, y_t, 2H - h_t) \to (x_2, y_2, h_2)\\
\text{left plane image point}: &\quad (-x_t, y_t, h_t) \to (x_3, y_3, h_3)\\
\text{right plane image point}: &\quad (2L_1 - x_t, y_t, h_t) \to (x_4, y_4, h_4)\\
\text{front plane image point}: &\quad (x_t, -y_t, h_t) \to (x_5, y_5, h_5)\\
\text{back plane image point}: &\quad (x_t, 2W_1 - y_t, h_t) \to (x_6, y_6, h_6)
\end{aligned} \tag{1}$$

Herein, point (x_0, y_0, h_0) represents the coordinate of the transmitting antenna; meanwhile, points $(x_\alpha, y_\alpha, z_\alpha)$, $\alpha = 1, 2, \cdots, 6$ describe the coordinates of the image points of the transmitting antennas with respect to different planes. Their subscripts α mean different planes, and they can be $1, 2, \cdots, 6$, representing the floor, ceiling, front wall, back wall, left wall, or right wall, respectively.

The electric fields of electromagnetic waves are highly dependent on their traveled distances. Hence, the path loss will be affected by the lengths of dominant rays, including *direct ray*, *reflected rays*, *diffracted ray*, *reflected-diffracted rays*, and *reflected-reflected ray*. Therefore, first of all, we should calculate these lengths.

As depicted in Fig. 1(a), $d_0(x_r, y_r, h_r)$ is the length of *direct ray*, and $d_\alpha(x_r, y_r, h_r)$, $\alpha = 1, 2, \cdots, 6$ are the lengths of *reflected rays*. $d_0(x_r, y_r, h_r)$ is given by

$$d_0(x_r, y_r, h_r) = \sqrt{(x_0 - x_r)^2 + (y_0 - y_r)^2 + (h_0 - h_r)^2} \tag{2}$$

In addition, as an example, Fig. 3(a) illustrates the length of the ray reflected by the floor based on the method of images. It equals the length between the image point (x_1, y_1, h_1) and receiving point (x_r, y_r, h_r). That is $\sqrt{(x_1 - x_r)^2 + (y_1 - y_r)^2 + (h_1 - h_r)^2}$. Similarly, $d_\alpha(x_r, y_r, h_r)$, $\alpha = 1, 2, \cdots, 6$ are given by

$$d_\alpha(x_r, y_r, h_r) = \sqrt{(x_\alpha - x_r)^2 + (y_\alpha - y_r)^2 + (h_\alpha - h_r)^2}, \quad \alpha = 1, 2, \cdots, 6 \tag{3}$$

To simplify the expressions, we define a function $d_\alpha(x, y, z)$, which describes the distance between point (x, y, z) and transmitting points or its image points for different reflection planes $(x_\alpha, y_\alpha, h_\alpha)$. It is expressed as:

$$d_\alpha(x, y, z) = \sqrt{(x_\alpha - x)^2 + (y_\alpha - y)^2 + (h_\alpha - z)^2}, \quad \alpha = 0, 1, 2, \cdots, 6 \tag{4}$$

Moreover, an illustration of the ray diffracted by the corner is presented in Fig. 3(b). The total lengths of the *diffracted ray* or *reflected-diffracted rays* are the sum of the distance from $(x_\alpha, y_\alpha, h_\alpha)$ to

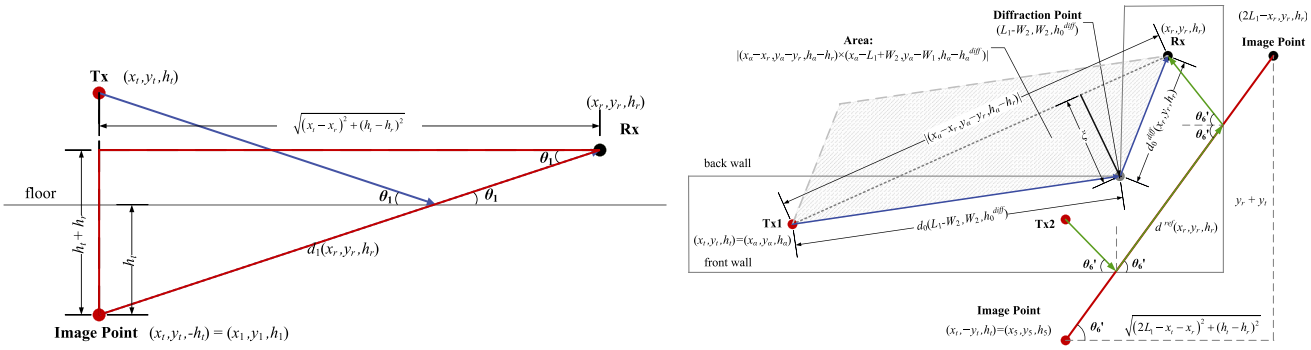

(a) (b)

Figure 3. Examples for the reselected and diffracted rays: (a) the ray reflected by the floor and (b) the ray diffracted by the corner and the ray reflected by the front and right wall.

the diffraction point $(L_1 - W_2, W_1, h_\alpha^{diff})$ and the one from the diffraction point $(L_1 - W_2, W_1, h_\alpha^{diff})$ to the receiving point (x_r, y_r, h_r). Herein, h_α^{diff}, $\alpha = 0, 1, \cdots, 5$ are the heights of the diffraction points. The former term can be calculated by $d_\alpha(L_1 - W_2, W_1, h_\alpha^{diff})$ using (4). The latter term is denoted as $d_\alpha^{diff}(x_r, y_r, h_r)$ as (5). The distances between the diffraction points $(L_1 - W_2, W_1, h_\alpha^{diff})$, $\alpha = 0, 1, 2, \cdots, 5$ and points (x, y, z), i.e., $d_\alpha^{diff}(x, y, z)$, are given by

$$d_\alpha^{diff}(x, y, z) = \sqrt{[x - (L_1 - W_2)]^2 + (y - W_1)^2 + \left(z - h_\alpha^{diff}\right)^2}, \quad \alpha = 0, 1, 2, \cdots, 5 \tag{5}$$

It is seen that the diffraction occurs at the corner of the environments as shown in Fig. 1(b); thus, its coordinate in the horizontal plane is fixed, i.e., $(L_1 - W_2, W_1)$. However, the heights of diffraction points are unknown and should be determined. According to the Fermat principle, electromagnetic waves will pass over the shortest path in the environment. The total lengths of the *diffracted ray* and *diffracted-reflected rays* are expressed as:

$$\begin{aligned} D\left(h_\alpha^{diff}\right) &= d_\alpha(L_1 - W_2, W_1, h_\alpha^{diff}) + d_\alpha^{diff}(x_r, y_r, h_r) \\ &= \sqrt{[x_\alpha - (L_1 - W_2)]^2 + (y_\alpha - W_1)^2 + (h_t - h_\alpha^{diff})^2} \\ &\quad + \sqrt{[x_r - (L_1 - W_2)]^2 + (y_r - W_1)^2 + (h_r - h_\alpha^{diff})^2}, \quad \alpha = 0, 1, 2, \cdots, 5 \end{aligned} \tag{6}$$

The shortest path can be obtained when $\partial D(h_\alpha^{diff})/\partial h_\alpha^{diff} = 0$. Then, we can get:

$$h_\alpha^{diff} = \frac{2R_\alpha^2(x_r, y_r)\, h_\alpha - 2T_\alpha^2(x_\alpha, y_\alpha)\, h_r - \sqrt{4T^2(x_\alpha, y_\alpha)\, R_\alpha^2(x_r, y_r)\, (h_\alpha - h_r)^2}}{2\left[R_\alpha^2(x_r, y_r) - T_\alpha^2(x_\alpha, y_\alpha)\right]}, \quad \alpha = 0, 1, 2, \cdots, 5 \tag{7}$$

where $T_\alpha(x_\alpha, y_\alpha)$ and $R_\alpha(x_r, y_r)$ are distances between (x_α, y_α) or (x_r, y_r) and $(L_1 - W_2, W_1)$ in horizontal planes:

$$\begin{aligned} T_\alpha(x_\alpha, y_\alpha) &= \sqrt{[x_\alpha - (L_1 - W_2)]^2 + (y_\alpha - W_1)^2}, \quad \alpha = 0, 1, 2, \cdots, 5 \\ R_\alpha(x_r, y_r) &= \sqrt{[x_r - (L_1 - W_2)]^2 + (y_r - W_1)^2}, \quad \alpha = 0, 1, 2, \cdots, 5 \end{aligned} \tag{8}$$

Figure 1(b) shows the ray reflected by the front and right walls as well. We can calculate the length of the *reflected-reflected rays* by the distance between the front plane image point of the Tx2 and the right plane image point of the Rx. It is given by

$$d^{ref}(x_r, y_r, h_r) = \sqrt{(2L_1 - x_t - x_r)^2 + (y_t + y_r)^2 + (h_t - h_r)^2} \tag{9}$$

2.2. Electric Fields for Line-of-Sight Condition

The *direct ray* and *reflected rays* are the dominant components for the LOS condition. Their electric fields at receiving points (x_r, y_r, h_r) are expressed as:

$$\begin{aligned} E_0^{LOS}(x_r, y_r, h_r) &= E_0 \left(\frac{\lambda}{4\pi}\right) \frac{e^{-j2\pi \frac{d_0(x_r, y_r, h_r)}{\lambda}}}{d_0(x_r, y_r, h_r)} \\ E_\alpha^{LOS}(x_r, y_r, h_r) &= E_0 \Gamma_\alpha(\theta_\alpha) \left(\frac{\lambda}{4\pi}\right) \frac{e^{-j2\pi \frac{d_\alpha(x_r, y_r, h_r)}{\lambda}}}{d_\alpha(x_r, y_r, h_r)} \end{aligned} \tag{10}$$

where E_0 is the original electric field at the transmitting point. $E_0^{LOS}(x_r, y_r, h_r)$ is the electric field of the direct ray at the receiving point for the LOS condition. $E_\alpha^{LOS}(x_r, y_r, h_r)$, $\alpha = 1, 2, \cdots, 6$ are the electric fields of the reflected waves at the receiving points, and λ denotes the wavelength of the electromagnetic waves. $d_\alpha(x_r, y_r, h_r)$, $\alpha = 0, 1, 2, \cdots, 6$ are the lengths of the *direct ray* and *reflected*

rays from the transmitting to receiving antennas, which can be calculated by (4). In (10), the symbols, $\Gamma_\alpha(\theta_\alpha)$, $\alpha = 1, 2, \cdots, 6$, represent the reflection coefficients of different planes, and they are given by

$$\Gamma_\alpha(\theta_\alpha) = \frac{\sin\theta_\alpha - X_\alpha(\theta_\alpha)}{\sin\theta_\alpha + X_\alpha(\theta_\alpha)}, \quad \alpha = 1, 2, \cdots, 6 \tag{11}$$

where the subscript α of Γ means the different walls, and θ_α is the angle between the reflection planes and the incident wave. $X_\alpha(\theta_\alpha)$ is:

$$\begin{aligned} X_\alpha(\theta_\alpha) &= \frac{\sqrt{\varepsilon_{r,\alpha} - \cos^2\theta_\alpha}}{\varepsilon_{r,\alpha}}, \text{ for verital polarization} \\ X_\alpha(\theta_\alpha) &= \sqrt{\varepsilon_{r,\alpha} - \cos^2\theta_\alpha}, \text{ for horizontal polarization} \end{aligned} \tag{12}$$

where $\varepsilon_{r,\alpha}$, $\alpha = 1, 2, \cdots, 6$ are the relative permittivity constants of the reflection planes. For example, Fig. 3(a) shows the method for calculating the sine and cosine values ($\cos\theta_1$ and $\sin\theta_1$) of the angle between the incident wave and the floor. Based on the same method, the sine and cosine values of all the angles, i.e., $\cos\theta_\alpha$ and $\sin\theta_\alpha$, can be calculated as:

$$\begin{aligned} \cos\theta_1 &= \frac{\sqrt{(x_1 - x_r)^2 + (y_1 - y_r)^2}}{d_1(x_r, y_r, h_r)}, \quad \sin\theta_1 = \frac{|h_r - h_1|}{d_1} \\ \cos\theta_2 &= \frac{\sqrt{(x_2 - x_r)^2 + (y_2 - y_r)^2}}{d_2(x_r, y_r, h_r)}, \quad \sin\theta_2 = \frac{|h_r - h_2|}{d_2} \\ \cos\theta_3 &= \frac{\sqrt{(y_3 - y_r)^2 + (h_3 - h_r)^2}}{d_3(x_r, y_r, h_r)}, \quad \sin\theta_3 = \frac{|x_r - x_3|}{d_3} \\ \cos\theta_4 &= \frac{\sqrt{(y_4 - y_r)^2 + (h_4 - h_r)^2}}{d_4(x_r, y_r, h_r)}, \quad \sin\theta_4 = \frac{|x_r - x_4|}{d_4} \\ \cos\theta_5 &= \frac{\sqrt{(x_5 - x_r)^2 + (h_5 - h_r)^2}}{d_5(x_r, y_r, h_r)}, \quad \sin\theta_5 = \frac{|y_r - y_5|}{d_5} \\ \cos\theta_6 &= \frac{\sqrt{(x_6 - x_r)^2 + (h_6 - h_r)^2}}{d_6(x_r, y_r, h_r)}, \quad \sin\theta_6 = \frac{|y_r - y_6|}{d_6} \end{aligned} \tag{13}$$

Then, we can simplify the equations in (13) by introducing parameters A, B, and C:

$$\begin{aligned} \cos\theta_\alpha &= \frac{\sqrt{A(x_\alpha - x_r)^2 + B(y_\alpha - y_r)^2 + C(h_\alpha - h_r)^2}}{d_\alpha(x_r, y_r, h_r)} \\ \sin\theta_\alpha &= \frac{(1-A)|x_\alpha - x_r| + (1-B)|y_\alpha - y_r| + (1-C)|h_\alpha - h_r|}{d_\alpha(x_r, y_r, h_r)} \end{aligned} \tag{14}$$

where $\alpha = 1, 2$ corresponds to $A = 1, B = 1, C = 0$; $\alpha = 3, 4$ corresponds to $A = 0, B = 1, C = 1$; $\alpha = 5, 6$ corresponds to $A = 1, B = 0, C = 1$.

2.3. Electric Fields for Non-Line-of-Sight Condition

Typically, there are corners in many indoor environments, for example, the "L-shaped" corridor environment. They will obstruct the direct LOS ray between the transmitting and receiving antennas, leading to a variation in the total path loss. Thus, the path loss characteristics for the NLOS conditions

would be different. The electric fields for the NLOS conditions are:

$$
\begin{aligned}
E_0^{NLOS}(x_r,y_r,h_r) &= E_0\left(\frac{\lambda}{4\pi}\right)\frac{L_0^{diff}\left(v(x_r,y_r,h_r)\right)e^{-j2\pi\frac{d_0\left(L_1-W_2,W_1,h_0^{diff}\right)+d_0^{diff}(x_r,y_r,h_r)}{\lambda}}}{d_0\left(L_1-W_2,W_1,h_0^{diff}\right)+d_0^{diff}\left(x_r,y_r,h_r\right)}\\
E_\alpha^{NLOS}(x_r,y_r,h_r) &= E_0\Gamma_\alpha(\theta_\alpha^{'})\left(\frac{\lambda}{4\pi}\right)\frac{L_\alpha^{diff}\left(v(x_r,y_r,h_r)\right)e^{-j2\pi\frac{d_\alpha\left(L_1-W_2,W_1,h_\alpha^{diff}\right)+d_\alpha^{diff}(x_r,y_r,h_r)}{\lambda}}}{d_\alpha\left(L_1-W_2,W_1,h_\alpha^{diff}\right)+d_\alpha^{diff}\left(x_r,y_r,h_r\right)}\\
E_6^{NLOS}(x_r,y_r,h_r) &= E_0\Gamma_5\left(\theta_6^{'}\right)\cdot\Gamma_4\left(\frac{\pi}{2}-\theta_6^{'}\right)\left(\frac{\lambda}{4\pi}\right)\frac{e^{-j2\pi\frac{d^{ref}(x_r,y_r,h_r)}{\lambda}}}{d^{ref}\left(x_r,y_r,h_r\right)}
\end{aligned}
\tag{15}
$$

where E_0 is the transmitted electric field. $E_0^{NLOS}(x_r,y_r,h_r)$, $E_\alpha^{NLOS}(x_r,y_r,h_r)$, $\alpha=1,2,\cdots,5$, and $E_6^{NLOS}(x_r,y_r,h_r)$ are the electric fields of the *diffracted ray*, *reflected-diffracted rays*, and *reflected-reflected ray*, respectively. $d_\alpha(L_1-W_2,W_1,h_\alpha^{diff})$, $\alpha=0,1,2,\cdots,5$ are the lengths of the rays from the transmitting antennas to the diffraction points $(L_1-W_2,W_1,h_\alpha^{diff})$. They can be calculated by (4). $d_\alpha^{diff}(x_r,y_r,h_r)$, $\alpha=0,1,2,\cdots,5$ are the lengths of the rays from the diffraction points to the receiving antennas, which can be determined by (5). $\Gamma_\alpha(\theta_\alpha^{'})$ describes the reflection coefficients for different planes which is similar to (11), (12), (14), where $\theta_\alpha^{'}$, $\alpha=0,1,2,\cdots,5$ are the angle between the wall and the incident wave for the NLOS conditions. Notably, the coordinates x_r, y_r, and h_r in (14) should be substituted by L_1-W_2, W_1, and h_α^{diff}, because the rays will travel through diffraction points $(L_1-W_2,W_1,h_\alpha^{diff})$. $\Gamma_5(\theta_6^{'})$ and $\Gamma_4(\pi/2-\theta_6^{'})$ are the reflection coefficients of the front and right walls, where $\theta_6^{'}$ is the angle between the front wall and the incident wave. $L_\alpha^{diff}(v(x_r,y_r,h_r))$ means the diffraction attenuations as (17).

As shown in Fig. 3(b), the cosine and sine values of $\theta_6^{'}$, i.e., $\cos\theta_6^{'}$ and $\sin\theta_6^{'}$, can be calculated by

$$
\cos\theta_6^{'}=\frac{\sqrt{(2L_1-x_t-x_r)^2+(h_t-h_r)^2}}{d^{ref}(x_r,y_r,h_r)},\quad \sin\theta_6^{'}=\frac{y_t+y_r}{d^{ref}(x_r,y_r,h_r)} \tag{16}
$$

The diffraction attenuations $L_\alpha^{diff}(v(x_r,y_r,h_r))$ can be approximately estimated by the Lee model [23]:

$$
L_\alpha^{diff}\left(v(x_r,y_r,h_r)\right)=\begin{cases}0.5-0.62v(x_r,y_r,h_r) & ,\ -0.8\le v(x_r,y_r,h_r)<0\\ 0.5e^{-0.95v(x_r,y_r,h_r)} & ,\ 0\le v(x_r,y_r,h_r)<1\\ 0.4-\sqrt{0.1184-\left[0.38-0.1v(x_r,y_r,h_r)\right]^2} & ,\ 1\le v(x_r,y_r,h_r)<2.4\\ 0.225/v(x_r,y_r,h_r) & ,\ v(x_r,y_r,h_r)>2.4\end{cases} \tag{17}
$$

In (17), $v(x_r,y_r,h_r)$ is the Fresnel-Kirchoff diffraction parameter and is given by

$$
\begin{aligned}
v(x_r,y_r,h_r) &= \xi\sqrt{\frac{2\left[d_\alpha\left(L_1-W_2,W_1,h_\alpha^{diff}\right)+d_\alpha^{diff}\left(x_r,y_r,h_r\right)\right]}{\lambda d_\alpha\left(L_1-W_2,W_1,h_\alpha^{diff}\right)d_\alpha^{diff}\left(x_r,y_r,h_r\right)}}\\
&= \pm\frac{\left|\left(x_\alpha-x_r,y_\alpha-y_r,h_\alpha-h_r\right)\times\left(x_\alpha-L_1+W_2,y_\alpha-W_1,h_\alpha-h_\alpha^{diff}\right)\right|}{\left|\left(x_\alpha-x_r\right),\left(y_\alpha-y_r\right),\left(h_\alpha-h_r\right)\right|}\\
&\quad\cdot\sqrt{\frac{2\left[d_\alpha\left(L_1-W_2,W_1,h_\alpha^{diff}\right)+d_\alpha^{diff}\left(x_r,y_r,h_r\right)\right]}{\lambda d_\alpha\left(L_1-W_2,W_1,h_\alpha^{diff}\right)d_\alpha^{diff}\left(x_r,y_r,h_r\right)}}
\end{aligned}
\tag{18}
$$

where ξ is the distance from the diffraction point $(L_1-W_2,W_1,h_\alpha^{diff})$ to the straight line through the points $(x_\alpha,y_\alpha,h_\alpha)$ and (x_r,y_r,h_r). It is a positive value when there is a LOS ray between $(x_\alpha,y_\alpha,h_\alpha)$

and (x_r, y_r, h_r), and conversely, it is negative when the LOS ray is obstructed. The operation $\times$ means the cross product of the vectors, and $|\cdot|$ means the Euclidean norm of the vector.

2.4. 3D Multi-Rays Path Loss Model

The received signals will be constructed and destructed by the electric fields of multiple arrived rays. By combining their electric fields, the total electric fields at the receiving points, i.e., $E_{total}^{LOS}(x_r, y_r, h_r)$ and $E_{total}^{NLOS}(x_r, y_r, h_r)$, can be obtained:

$$\begin{aligned} E_{total}^{LOS}(x_r, y_r, h_r) &= E_0^{LOS}(x_r, y_r, h_r) + \sum_{\alpha=1}^{6} E_\alpha^{LOS}(x_r, y_r, h_r) \\ E_{total}^{NLOS}(x_r, y_r, h_r) &= E_0^{NLOS}(x_r, y_r, h_r) + \sum_{\alpha=1}^{5} E_\alpha^{NLOS}(x_r, y_r, h_r) + \delta \cdot E_6^{NLOS}(x_r, y_r, h_r) \end{aligned} \tag{19}$$

where $E_\alpha^{LOS}(x_r, y_r, h_r)$, $\alpha = 0, 1, \cdots, 6$ and $E_\alpha^{NLOS}(x_r, y_r, h_r)$, $\alpha = 0, 1, \cdots, 6$ are the electric fields of different rays. They can be calculated by (10) and (15) in Sections 2.2–2.3. The parameter δ is used for distinguishing whether the Tx is near the corner or not. The *reflected-reflected ray* will not exist when the line between $(x_t, -y_t, h_r)$ and $(2L_1 - x_r, y_r, h_r)$ is obstructed by the back wall. Herein, δ is 0; otherwise, δ is 1, because the *reflected-reflected ray* should obey the law of reflection.

Path loss describes the quotient of transmitting power and receiving power. It is the large scale characteristic of the channel. Thus, in the proposed model, the electric fields should be squared to obtain the power, and the small scale properties should be eliminated by averaging the power in a small area. Then, by dividing the square of the transmitted electric field $|E_0|^2$ by the square of the received electric field $|E_{total}^{LOS}(x_r, y_r, h_r)|^2$ or $|E_{total}^{NLOS}(x_r, y_r, h_r)|^2$, and averaging the results in a small area, the path loss in decibel can be calculated by

$$\begin{aligned} PL^{LOS}(x_r, y_r, h_r) &= 10\lg\left[\frac{1}{N}\sum_{\Phi(x,y,h)\le S}\frac{|E_0|^2}{\left|E_{total}^{LOS}(x,y,h)\right|^2}\right] \\ &= -10\lg\left[\frac{1}{N}\sum_{\Phi(x,y,h)\le S}\left|\sum_{\alpha=0}^{6}\frac{\Xi_\alpha e^{-j2\pi\frac{d_\alpha(x_r,y_r,h_r)}{\lambda}}}{d_\alpha(x_r, y_r, h_r)}\right|^2\right] \end{aligned} \tag{20}$$

$$\begin{aligned} PL^{NLOS}(x_r, y_r, h_r) &= 10\lg\left[\frac{1}{N}\sum_{\Phi(x,y,h)\le S}\frac{|E_0|^2}{\left|E_{total}^{NLOS}(x,y,h)\right|^2}\right] \\ &= -10\lg\left[\frac{1}{N}\sum_{\Phi(x,y,h)\le S}\left|\begin{array}{l}\displaystyle\sum_{\alpha=0}^{5}\frac{\Psi_\alpha e^{-j2\pi\frac{d_\alpha(L_1-W_2,W_1,h_\alpha^{diff})+d_\alpha^{diff}(x_r,y_r,h_r)}{\lambda}}}{d_\alpha(L_1-W_2,W_1,h_\alpha^{diff})+d_\alpha^{diff}(x_r,y_r,h_r)} \\ \displaystyle+\delta\cdot\Gamma_5\left(\theta_6'\right)\Gamma_4\left(\frac{\pi}{2}-\theta_6'\right)\frac{e^{-j2\pi\frac{d^{ref}(x_r,y_r,h_r)}{\lambda}}}{d^{ref}(x_r,y_r,h_r)}\end{array}\right|^2\right] \end{aligned} \tag{21}$$

where $PL^{LOS}(x_r, y_r, h_r)$ and $PL^{NLOS}(x_r, y_r, h_r)$ are the path loss for the LOS and NLOS conditions, respectively. $\Phi(x, y, h)$ is the distance between the point (x, y, h) and (x_r, y_r, h_r), that is $\Phi(x, y, h) = |(x - x_r, y - y_r, h - h_r)|$, where $|\cdot|$ is the Euclidean norm of the vector. S represents the radius of the small area in order to remove the small scale fading. N is the number of points in this area. Ξ_α and Ψ_α are

$$\Xi_\alpha = \begin{cases} \left(\frac{\lambda}{4\pi}\right)^2, & \alpha = 0 \\ \left(\frac{\lambda}{4\pi}\right)^2 \Gamma_\alpha(\theta_\alpha), & \alpha = 1, \cdots, 6 \end{cases}, \Psi_\alpha = \begin{cases} \left(\frac{\lambda}{4\pi}\right)^2 L_0^{diff}\left(v(x_r, y_r, h_r)\right), & \alpha = 0 \\ \left(\frac{\lambda}{4\pi}\right)^2 \Gamma_\alpha(\theta_\alpha') L_\alpha^{diff}\left(v(x_r, y_r, h_r)\right), & \alpha = 1, \cdots, 5 \end{cases} \tag{22}$$

Finally, as (20) and (21), a multi-rays path loss model is proposed. To summarize, the model parameters can be categorized into 6 types: (1) the size of the environments, i.e., L_1, L_2, W_1, W_2, H; (2) the position of the transmitting antenna, i.e., x_t, y_t, h_t; (3) the property of the electromagnetic waves, i.e., λ; (4) the permittivity constants of different the walls, i.e., $\varepsilon_{r,\alpha}$, $\alpha = 1, 2, \cdots, 6$; (5) the radius of the small area, i.e., S; (6) the parameter describes whether the transmitting antenna is near or far away from the corner, i.e., δ. These parameters will comprehensively affect the performance of the proposed model. Notably, the proposed model is used for describing path loss under indoor environments with a regular structure. The ceilings, floors, and walls may vary with the environment. For example, many buildings have suspended ceilings of acoustic tiles. The reflection caused by this type of ceiling is quite weak. Thus, the item $\alpha = 2$ in the inner summation of (20)–(21) should not be included in this case. In contrast, if the environment is furnished with ordinary ceilings, such as a gypsum ceiling, the item $\alpha = 2$ should be reserved.

As shown in (20) and (21), compared with the distance-dependent path loss models, all path losses in the 3D spaces can be characterized by the proposed model since they are the functions of the coordinates (x_r, y_r, h_r). In addition, the proposed model considers multiple dominant rays for both the LOS and NLOS conditions. Moreover, it contains information about the locations of the transmitting antennas, sizes and materials of the environments, and the wavelength of the electromagnetic waves.

3. EXPERIMENTS AND MODEL VALIDATION

3.1. Measurement Environments and Measurement Campaigns

Extensive channel measurements above 6 GHz are carried out for model validation. We collect the measured data under two real indoor environments in an office building, i.e., the empty "L-shaped" corridor and squared office. Fig. 4 exhibits the plane views of the measured environments. Both environments consist of concrete walls, gypsum ceilings, and tiled floors. The sizes of the corridor and office are measured and tabulated in Table 2, where the meaning of the symbols, i.e., L_1, L_2, W_1, W_2, and H, are the same as the ones shown in Fig. 1. The total plane areas of the two environments are $81\,\mathrm{m}^2$ and $64\,\mathrm{m}^2$.

The channel sounding system conducts the measurements, and its elaborate information can be found in [24]. The Vector Network Analyzer (VNA), the system's core equipment, serves as a

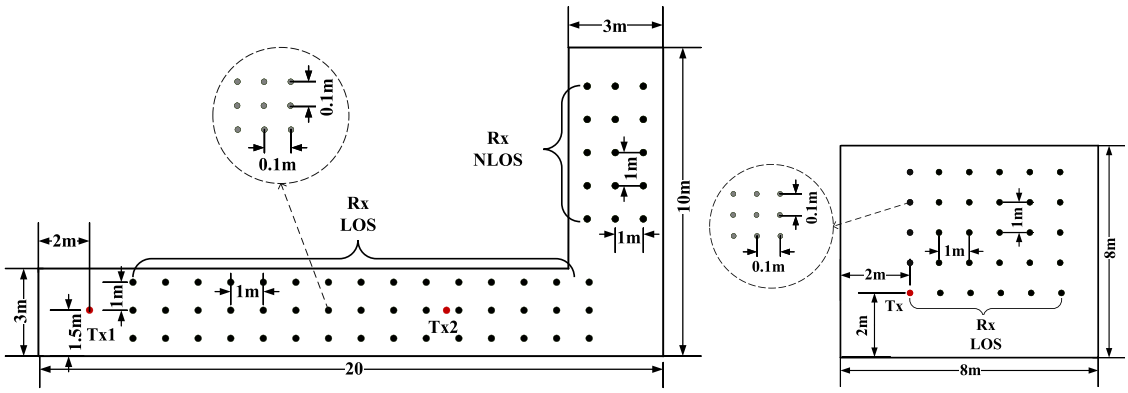

Figure 4. The measured environments: (a) corridor and (b) office.

Table 2. The sizes of the measured corridor and office.

Environments	L_1	L_2	W_1	W_2	H
Corridor	20 m	10 m	3 m	3 m	4 m
Office	8 m	8 m	8 m	8 m	4 m

synchronous transceiver. The two ports of the VNA are connected to two omnidirectional monopole antennas via two low loss cables. The system can obtain the channel frequency response by capturing the S_{21} parameters of the VNA. The VNA sweeps from 7.5 GHz to 8.5 GHz, and its transmitting power is 10 dBm. The measured center frequency is 8 GHz, and its wavelength, i.e., λ, is 0.0375 m. The measurements are carried out in the environments as shown in Fig. 4. To validate the proposed model in the situations where the transmitting antenna is far away from or near the corner of the corridor, the transmitting antenna is placed in two different places marked as Tx1 and Tx2 with a height of 3.5 m in Fig. 4(a). In addition, it is placed at the place marked as Tx with a height of 3.9 m in the office environment, as represented in Fig. 4(b). The receiving antenna is placed on the tripod and moved to different Rx points as denoted in Figs. 4(a) and (b) with heights of 1.6 m and 0.6 m. At each receiving point, the measurements are conducted at nine different grid points with an interval of 0.1 m. As an example, Fig. 4 also shows the deployment of the grid point. We repeat the measurements, i.e., a complete sweep period of the VNA, ten times at each grid point. In addition, the sweep period of the VNA is 400 ms; thus, the measured environments are kept to be static during each sweep. The elaborate configurations of the measurement campaigns are listed in Table 3.

Table 3. The configurations of the measurement campaigns.

Item	Configuration
Model of VNA	Agilent 8720ES
Transmitting power	10 dBm
Sweep frequency band	7.5 GHz–8.5 GHz
Number of sweep points	201
Sweep period	400 ms
Type of antennas	Omnidirectional monopole
Gain of antennas	3 dBi
Polarization of antennas	Vertical
Attenuation of cables	0.6 dB/m
Length of cables	20 m
Height of transmitting antenna	3.5 m(corridor), 3.9 m(office)
Height of receiving antenna	1.6 m(corridor), 0.6 m(office)
Number of receiving points	60(corridor), 35(office)
Number of grid points	9(corridor), 9(office)

3.2. Model Validation

The above measurement campaigns can obtain extensive channel frequency responses. We convert them into path loss using the method in [25]. It is notable that the measured path losses are averaged over the nine grid points and ten repeated samples at each receiving point to remove the influences of noise and small scale fading. Then, we can use them to validate the proposed path loss model. Herein, three widely used path loss models, including the log-distance model [22], dual-slopes model [26], and two-rays model [27], are used as reference models for comparison. Usually, these models are widely used in indoor corridor and office environments.

As per the measurement environments and campaigns, the parameters of the proposed model are set out in Table 4. The size of the environments can be found in Table 2. The permittivity constants of the different walls can refer to [22, 28, 29]. The small scale fading describes the signal variations within a short range, such as ten wavelengths. Thus, to eliminate the small scale fading, the radius of the small area can be set as a value slightly bigger than ten wavelengths, that is 0.4 m. Then, using these model parameters, we can generate the path loss by the proposed model. In addition, the ceilings of

Table 4. The parameters of the proposed path loss model.

Environment	L_1, L_2, W_1, W_2, H	x_t (m)	y_t (m)	h_t (m)	λ (m)	$\varepsilon_{r,1}$	$\varepsilon_{r,2}$	$\varepsilon_{r,3}$	$\varepsilon_{r,4}$	$\varepsilon_{r,5}$	$\varepsilon_{r,6}$	S (m)	δ
Corridor Tx1	c.f. Table 2	2	1.5	3.5	0.0375	9	2.5	6	6	6	6	0.4	0
Corridor Tx2	c.f. Table 2	13.5	1.5	3.5	0.0375	9	2.5	6	6	6	6	0.4	1
Office	c.f. Table 2	2	2	3.9	0.0375	9	2.5	6	6	6	6	0.4	0

the measured corridor and office are gypsum ceilings. Therefore, the reflections caused by the ceiling are considered, that is $\alpha = 2$ in (20)–(21) should be contained.

Figures 5(a)–(c) draw the scatter plots of the measured path loss and the curves of the proposed multi-rays path loss model, log-distance path loss model, dual slopes path loss model, and 2-rays path loss model for different cases. The first and second cases are in the corridor environment, when the transmitting antenna is far away from or near the corner, as shown in Fig. 5(a) and Fig. 5(b), respectively. The third case is in the office environment, as depicted in Fig. 5(c). In Fig. 5(a), it is seen that in the corridor environment, with the increase of the distance, the path loss increases at first, then it tends to be a stable value for the LOS condition. In other words, there is a breakpoint in the path loss for the LOS conditions. This phenomenon is consistent with the results in [30]. Additionally, the fluctuations can be found for the measured path loss. They are caused by the construction and destruction of electromagnetic waves at different places. For the NLOS conditions, the path loss increases with the distance as well. Such increases are faster than the ones for the LOS conditions. Additionally, the path loss fluctuations are much more significant than the LOS conditions due to the absence of the direct ray. The transmuting antenna is near the corner of the corridor in Fig. 5(b). It is noteworthy that the difference between Fig. 5(a) and Fig. 5(b) is caused by the position of the transmitting antenna. In this case, the existence of the *reflected-reflected ray* is considered for the NLOS condition. Moreover, since the transmitting antenna is near the corner, the overall distances are smaller than in the former case. Thus, the breakpoint is missing. Fig. 5(c) shows the path loss in the office environment. The results show that all the measured points are for the LOS conditions. The direct ray will dominate the overall variation trends of the path loss. Thus, it can be found that the path loss increases with the distance. In addition, fluctuations of the path loss can be observed in the proposed model because the reflected rays from different walls are generally in phase in some regions, giving rise to a max in the averaged path loss and generally out of phase in other regions, giving a min. In addition, the lengths of reflected rays increase fast at the other end of the office, compared with the direct ray. Therefore, the influence of the reflected ways on the path loss will become weak with the increase of the distance, leading to that the separation of the maxima and the minima is close when the receiving antenna is far from the transmitting antenna, but much larger when it is near the transmitting antenna. To verify this phenomenon, we separate multiple rays into the direct ray and all the reflected rays, and their path losses are drawn in Fig. 6. It can be found that the variation and fluctuation trends are consistent with

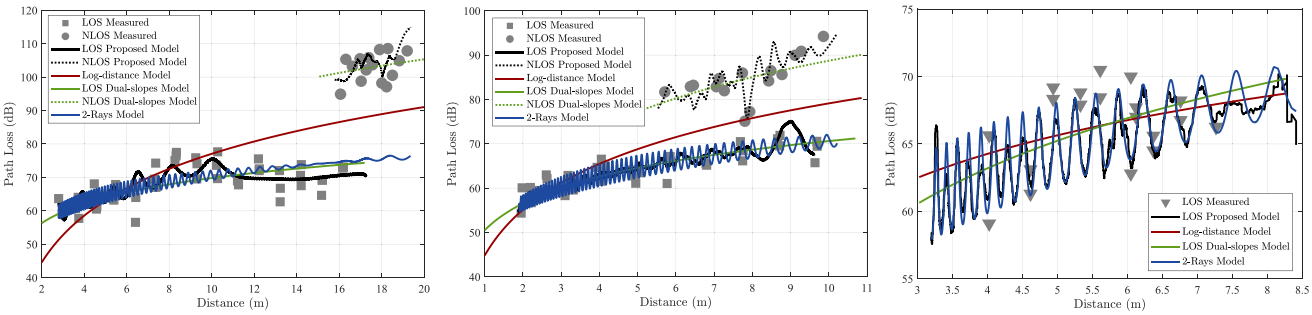

Figure 5. The measured data and the path loss models: (a) corridor (Tx is far away from corner), (b) corridor (Tx is near corner), and (c) office.

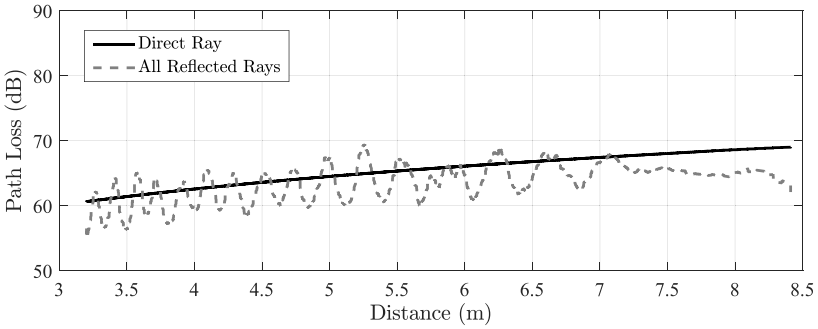

Figure 6. The path loss for the direct ray and all reflected rays under office environment.

our above analysis. Moreover, no break point can be observed because of the small separations of the transmitting and receiving antennas.

The overall results show that the proposed model can match the measured data under both the indoor corridor and office environments, verifying the extensibility of the proposed model. Although the plane views of the corridor and office environments are quite different, both can be depicted by the regular structure as depicted in Fig. 1. Moreover, the reference models deviate from the measured data. The reasons can be explained as follows. The log-distance path loss model has two parameters, i.e., the path loss exponent and reference path loss. It cannot distinguish the path loss between the LOS and NLOS conditions. The dual-slopes path loss model can describe the path loss for the LOS and NLOS conditions using two different path loss exponents. However, the fluctuations of the path loss at different places caused by the construction and destruction of the electromagnetic waves are hard to be characterized. The 2-rays path loss model only considers the direct ray and floor reflected ray in the environments, and the other dominant reflected or diffracted rays are ignored. Especially for the NLOS conditions, the direct ray is missing, leading to the mismatch between the 2-rays model and the measured data.

Furthermore, to quantitatively measure the fitness of the proposed model, the Minimum Square Errors (MSEs) between the measured data and the different path loss models are summarized in Table 5. The MSEs of the proposed path model are the smallest among all the path loss models under two different environments, verifying the accuracy and extensibility of the proposed model. One of the advantages of the proposed model is that it can describe both the variation trends with the distance and the fluctuation caused by the construction and destruction of the electric fields of different rays. In addition, the gap between the proposed model and empirical model, i.e., dual-slopes, is small. Hence, the proposed multi-rays path loss model can illustrate the propagation mechanisms of the dual-slopes model.

Table 5. The MSEs of different models.

Environment	Proposed Model	Log-distance Model	Dual-slopes Model	2-Rays Model
Corridor Tx1	0.52	1.45	0.55	1.87
Corridor Tx2	0.29	0.87	0.34	1.11
Office	0.6	0.6	0.61	0.65

In addition, the proposed model can directly calculate path loss by inputting or revising the model parameters. However, for general-purpose ray tracing programs, we should draw or import the digital map, set the electromagnetic parameters of the environment, then conduct the simulation. This process will be time-consuming. Moreover, we have compared the calculation time under the same environments using the proposed model and general-purpose ray tracing program, including the image and shooting and bouncing rays methods. The proposed model and ray tracing consume 1.865 s and 4.062 s/6.782 s to obtain the path loss, respectively. This result is because the general-purpose ray tracing program will consume much time to convert the digital map and electromagnetic parameters into the format

that the ray tracing solver can understand [20]. However, the proposed model directly uses the model parameters to calculate the path loss. Thus, the proposed model will be faster.

4. CONCLUSION

This paper presents a 3D multi-rays path loss model via analytical modeling. The detailed process for establishing the closed-form path loss formulas with clear propagation mechanisms is illustrated. In addition, the proposed model can describe the path loss everywhere in the 3D spaces because of the dependency on the coordinates. Its complexity is low because drawing digital maps and calculating lots of electromagnetic waves are unnecessary. Then, extensive measurements under an "L-shaped" corridor and squared office environments verify the proposed model. Compared with the conventional dual-slopes model, log-distance model, and 2-rays model, the proposed model exhibits high accuracy. In general, this model can serve as a fast and accurate solver for electromagnetic waves under regular-structured environments and is helpful for the link budget, node deployment, and coverage enhancement for future ubiquitous indoor communications at high frequency bands.

However, serval challenges and problems still exist. The influence of the scatters in the environments on path loss could be researched. Moreover, how to quantitatively study the model complexity of the path loss model is also essential. Lastly, the effects of the path loss model on the performance of the communications system, such as the coverage and the overall power cost, could be further investigated.

ACKNOWLEDGMENT

This work is supported by the Natural Science Foundation for Youths of Jiangsu Province (Grant No. BK20201044), Industry-University-Research Innovation Fund for Chinese Universities (Grant No. 2021FNA05002), National Nature Science Foundation of China (Grant No. 61871233) and High-Level Research Initiation Foundation for Introduction of Talents of Nanjing Institute of Technology (Grant Nos. YKJ201970 and YKJ201971).

REFERENCES

1. Panwar, N., S. Sharma, and A. K. Singh, "A survey on 5G: The next generation of mobile communication," *Physical Communication*, Vol. 18, 64–84, 2016.
2. Huang, T., W. Yang, J. Wu, X. Ma, X. F. Zhang, and D. Y. Zhang, "A survey on green 6G network: Architecture and technologies," *IEEE Access*, Vol. 7, 175758–175768, 2019.
3. Alabish, A., A. Goweder, and A. Dowa, "Measurement system and its suitability for examining indoor millimeter wave propagation at 28–33 GHz," *IEEE 1st International Maghreb Meeting of the Conference on Sciences and Techniques of Automatic Control and Computer Engineering, MI-STA*, 608–612, 2021.
4. Mohammed, I., A. M. Aibinu, and T. Karataev, "Overview of radio propagation models in the millimeter wave range for cellular networks," *IEEE International Conference on Multidisciplinary Engineering and Applied Science (ICMEAS)*, 1–6, 2021.
5. Hamdan, N. and B. K. Engiz, "A brief review of path loss models for mmwave channels," *Avrupa Bilim ve Teknoloji Dergisi*, No. 29, 264–272, 2021.
6. Al-Saman, A., M. Cheffena, O. Elijah, Y. A. Al-Gumaei, S. K. Abdul-Rahim, and T. Al-Hadhrami, "Survey of millimeter-wave propagation measurements and models in indoor environments," *Electronics*, Vol. 10, No. 14, 1653, 2021.
7. Shabbir, N., L. Kütt, M. M. Alam, P. Roosipuu, M. Jawad, M. B. Qureshi, A. R. Ansari, and R. Nawaz, "Vision towards 5G: Comparison of radio propagation models for licensed and unlicensed indoor femtocell sensor networks," *Physical Communication*, Vol.47, 101371, 2021.
8. Obeidat, H., A. Alabdullah, E. Elkhazmi, W. Suhaib, O. Obeidat, M. Alkhambashi, M. Mosleh, N. Ali, Y. Dama, Z. Abidin, R. Abd-Alhameed, and P. Excell, "Indoor environment propagation review," *Computer Science Review*, Vol. 37, 100272, 2020.

9. Alobaidy, H. A., M. J. Singh, M. Behjati, R. Nordin, and N. F. Abdullah, "Wireless transmissions, propagation and channel modelling for IoT technologies: Applications and challenges," *IEEE Access*, Vol. 10, 24095–24131, 2022.
10. Majed, M. B., T. A. Rahman, O. A. Aziz, M. N. Hindia, and E. Hanafi, "Channel characterization and path loss modeling in indoor environment at 4.5, 28, and 38 GHz for 5G cellular networks," *International Journal of Antennas and Propagation*, Vol. 2018, 2018.
11. Xing, Y., T. S. Rappaport, and A. Ghosh, "Millimeter wave and sub-THz indoor radio propagation channel measurements, models, and comparisons in an office environment," *IEEE Communications Letters*, Vol. 25, No. 110, 3151–3155, 2021.
12. Abbasi, N. A., A. Hariharan, A. M. Nair, and A. F. Molisch, "Channel measurements and path loss modeling for indoor THz communication," *IEEE European Conference on Antennas and Propagation (EuCAP)*, 1–5, 2020.
13. Song, Q., P. Tang, T. Jiang, L. Tian, J. Zhang, and J. Dou, "Modeling of path loss characteristics in a waveguide-like structure scenario at 28 GHz," *IEEE European Conference on Antennas and Propagation (EuCAP)*, 1–5, 2021.
14. Goes, A. A., P. Cardieri, and M. D. Yacoub, "Characterization of the RFID deterministic path loss in manufacturing environments," *IEEE 23rd International Symposium on Personal, Indoor and Mobile Radio Communications (PIMRC)*, 647–652, 2012.
15. Park, K. M., J. Y. Lee, S. H. Hyun, and S. C. Kim, "Analysis of path loss properties in indoor hallway with waveguide channel model," *IEEE VTS Asia Pacific Wireless Communications Symposium (APWCS)*, 1–5, 2019.
16. Li, S., Y. Liu, X. Zhang, and X. Qi, "Measurement and simulation of 28 GHz millimeter-wave propagation characteristics in the corridor environment," *IEEE 9th UK-Europe-China Workshop on Millimetre Waves and Terahertz Technologies (UCMMT)*, 134–137, 2016.
17. Bhuvaneshwari, A., R. Hemalatha, and T. Satyasavithri, "Path loss prediction analysis by ray tracing approach for NLOS indoor propagation," *IEEE International Conference on Signal Processing and Communication Engineering Systems*, 486–491, 2015.
18. Hossain, F., T. K. Geok, T. A. Rahman, M. N. Hindia, K. Dimyatiet, and A. Abdaziz, "Indoor millimeter-wave propagation prediction by measurement and ray tracing simulation at 38 GHz," *Symmetry*, Vol. 10, No. 10, 464, 2018.
19. Liu, J., D. W. Matolak, M. Mohsen, and J. Chen, "Path loss modeling and ray-tracing verification for 5/31/90 GHz indoor channels," *IEEE 90th Vehicular Technology Conference (VTC 2019-Fall)*, 1–6, 2019.
20. He, D., B. Ai, K. Guan, L. H. Wang, Z. D. Zhong, and K. Thomas, "The design and applications of high-performance ray-tracing simulation platform for 5G and beyond wireless communications: A tutorial," *IEEE Communications Surveys & Tutorials*, Vol. 21, No. 1, 10–27, 2018.
21. Guo, H., Z. Sun, and P. Wang, "Channel modeling of MI underwater communication using tri-directional coil antenna," *IEEE Global Communications Conference (GLOBECOM)*, 1–6, 2015.
22. Rappaport, T. S., *Wireless Communications — Principles and Practice*, 2nd Edition, Prentice Hall PTR, New Jersey, 2002.
23. Lee, W. C. Y., *Mobile Communications Engineering: Theory and Applications*, McGraw-Hill Publications, New York, 1998.
24. Yu, Y., P. F. Cui, W. J. Lu, Y. Liu, and H. B. Zhu, "Off-body radio channel impulse response model under hospital environment: Measurement and modeling," *IEEE Communications Letters*, Vol. 20, No. 11, 2332–2335, 2016.
25. Molina-Garcia-Pardo, J. M., C. Garcia-Pardo, J. V. Rodriguez, and L. Juan-Llacer, "Path loss and delay spread in UWB channels," *IEEE Antennas and Propagation Society International Symposium*, 1–4, 2009.
26. Oyie, N. O. and T. J. O. Afullo, "An empirical approach to omnidirectional path loss and line-of-sight probability models at 18 GHz for 5G networks," *2018 Progress In Electromagnetics Research Symposium (PIERS — Toyama)*, 129–136, Toyama, Japan, August 1–4, 2018.

27. Goldsmith, A., *Wireless Communications*, Cambridge University Press, Cambridge, 2005.
28. Olkkonen, M., V. Mikhnev, and E. Huuskonen-Snicker, "Complex permittivity of concrete in the frequency range 0.8 to 12 GHz," *IEEE European Conference on Antennas and Propagation (EuCAP)*, 3319–3321, 2013.
29. Grosvenor, C. A., R. T. Johnk, J. Baker-Jarvis, M. D. Janezic, and B. Riddle, "Time-domain free-field measurements of the relative permittivity of building materials," *IEEE Transactions on Instrumentation and Measurement*, Vol. 58, No. 7, 2275–2282, 2009.
30. Oyie, N. O. and T. J. O. Afullo, "Measurements and analysis of large-scale path loss model at 14 and 22 GHz in indoor corridor," *IEEE Access*, Vol. 6, 17205–17214, 2018.